ChemComm

COMMUNICATION

View Article Online
View Journal

Cite this: DOI: 10.1039/d6cc01492e

Received 12th March 2026,
Accepted 6th May 2026

DOI: 10.1039/d6cc01492e

rsc.li/chemcomm

A restructuring-resistant BiCuOS superlattice stabilizing Bi–O coordination for highly selective CO_2 electroreduction to formate

Ganwen Chen, †[ab] Jie Chen,†[cd] Yukun Xiao,[b] Meng Wang,[b] Yishui Ding,[b] Chenrui Ji,[b] Lei Fan,[b] Bailin Tian,[b] Changjin Guo,[b] Hexing Li,[e] Yuecheng Xiong,*[b] Zhangliu Tian*[bf] and Wei Chen *[bc]

Bismuth-based catalysts for eCO_2R often undergo restructuring, obscuring intrinsic activity. Here we report a restructuring-resistant BiCuOS catalyst with a stable and active Bi–O framework, delivering 96.6% $FE_{formate}$ at −0.7 V_{RHE} and enabling identification of *OCHO as the key intermediate and *HCOOH formation as the rate-determining step.

CO_2 emissions from human activities, particularly fossil fuel combustion and deforestation, have led to a continuous rise in atmospheric CO_2 levels, driving global warming and increasing the frequency of extreme weather events.[1] Converting CO_2 into value-added fuels and chemicals, such as formic acid, carbon monoxide, and alcohols, represents a promising approach to close the carbon cycle while addressing environmental and energy challenges.[2]

P-block elements, particularly Bi, Sn, and In, have attracted growing attention in electrocatalysis due to their unique p-orbital electronic configurations, low toxicity, and strong affinity toward oxygenated intermediates. Among them, Bi-based compounds are particularly promising for formate-selective electrochemical CO_2 reduction (eCO_2R) at low overpotentials.[3] However, despite their favorable thermodynamics, P-block metal oxides often suffer from spontaneous self-reduction and structural instability under cathodic conditions, resulting in performance deterioration and ambiguous identification of active sites.[4,5]

Among oxide-derived bismuth catalysts, Bi_2O_3 and $Bi_2O_2CO_3$ (BOC) have been extensively investigated for eCO_2R. Recent studies suggest that the geometry of the Bi–O coordination environment plays a decisive role in dictating catalytic performance.[6] In particular, catalytic materials adopting the *P*4/*nmm* space group, where Bi atoms are coordinated in tetrahedral Bi–O configurations, exhibit enhanced electronic properties and superior formate selectivity. This structural motif, exemplified by BOC, facilitates stabilization of reaction intermediates and suppresses the competing hydrogen evolution reaction (HER). However, under cathodic operating conditions, these oxidized Bi catalysts frequently undergo electrochemical reconstruction into metallic Bi, which promotes the HER and compromises selectivity. As a result, the intrinsic catalytic role of the Bi–O coordination environment remains poorly understood. Therefore, developing strategies to stabilize the Bi–O coordination environment against electrochemical reconstruction is critical for preserving catalytic selectivity and establishing reliable structure–activity relationships in Bi-based eCO_2R.

Quaternary Bi-based layered compounds, specifically BiMOCh (Ch = S, Se, Te; M = Cu, Ag), offer a promising strategy to mitigate the instability of Bi–O coordination under cathodic conditions, as their robust superlattice of alternating oxide and chalcogenide layers can effectively stabilize Bi–O sites. In addition, this layered architecture is widely reported to offer favorable electronic properties that can facilitate interfacial charge transfer during electrocatalysis.[7] Related layered oxysulfides (*e.g.*, LnCuOS, Ln = La, Pr, Nd) exhibit higher electrical conductivity than many other rare-earth oxysulfides, attributed to lowered conduction-band energies revealed by band-structure calculations.[8,9] These features motivate the exploration of quaternary Bi-based layered compounds as platforms for stabilizing Bi–O coordination and enabling efficient formate-selective eCO_2R.

[a] *Joint School of National University of Singapore and Tianjin University, International Campus of Tianjin University, Binhai New City, Fuzhou 350207, PR China*
[b] *Department of Chemistry, National University of Singapore, 3 Science Drive 3, 117543, Singapore. E-mail: xiongyc@nus.edu.sg, tianzhangliu@mail.sic.ac.cn, phycw@nus.edu.sg*
[c] *Department of Physics, National University of Singapore, 2 Science Drive 3, 117542, Singapore*
[d] *State Key Laboratory of Metal Organic Chemistry, Shanghai Institute of Organic Chemistry, Chinese Academy of Sciences, Shanghai, 200032, China*
[e] *The Education Ministry Key Lab of Resource Chemistry, Joint International Research Laboratory of Resource Chemistry of Ministry of Education, Shanghai Key Laboratory of Rare Earth Functional Materials, and Shanghai Frontiers Science Center of Biomimetic Catalysis, Shanghai Normal University, Shanghai 200234, China*
[f] *CAS Key Laboratory of Materials for Energy Conversion, Shanghai Institute of Ceramics, Chinese Academy of Sciences, Shanghai, 200050, PR China*
† Ganwen Chen and Jie Chen contributed equally to this work and share first authorship.

Herein, we present BiCuOS as a structurally robust and highly selective electrocatalyst for the electrochemical reduction of CO_2 to formate. Comprehensive characterizations reveal that the catalyst maintains its structural integrity and Bi oxidation state during extended operation. Notably, BiCuOS achieves over 90% faradaic efficiency for formate ($FE_{formate}$) across a wide potential range (-0.3 to -0.9 V_{RHE}), reaching a peak selectivity of 96.6% at -0.7 V_{RHE}. Electrolysis at industrial-level current density (100 mA cm^{-2}) exhibits stable performance for over 100 hours in alkaline electrolyte. Mechanistic investigations based on *in situ* ATR-SEIRAS and density functional theory (DFT) calculations identify *OCHO as the key intermediate, with a low energy barrier for its subsequent protonation. These findings establish BiCuOS as a structurally robust and mechanistically favorable platform for selective CO_2 to formate conversion under practical conditions.

BiCuOS nanosheets (NSs) were prepared from the direct solid state reaction method. Fig. 1a and Fig. S1 show the X-ray diffraction (XRD) patterns of the synthesized and acid-washed BiCuOS NSs, which are well indexed to the standard JCPDS reference pattern. The main BiCuOS framework is preserved after the washing step (Fig. S2).[8,10] Morphological characterization by scanning electron microscopy (SEM) shows a nanosheet architecture with etching marks (Fig. S3), which is further corroborated by transmission electron microscopy (TEM) (Fig. 1b). High-resolution TEM (HRTEM) images (Fig. 1c and Fig. S3) display clear lattice fringes with interplanar spacings of 0.274 and 0.284 nm, which can be indexed to the (110) and (102) planes of BiCuOS, respectively, indicating good crystallinity. The BiCuOS nanosheets are laterally extended within the ab plane, while the layers are stacked along [001]. The energy dispersive X-ray spectroscopy (EDS) elemental mapping images of BiCuOS confirm a uniform distribution of Bi, Cu, O and S elements throughout the whole NSs (Fig. 1d). To establish the local coordination environment of Bi, Bi L3-edge synchrotron radiation X-ray absorption spectroscopy (XAS) was collected (Fig. 1e–g). These results indicate oxygen-coordinated bismuth centers without detectable metallic Bi domains, supporting the successful synthesis of structurally well-defined BiCuOS.

The eCO_2R performance was tested in a flow-type reactor with a gas diffusion electrode (GDE) (Fig. S6). Linear sweep voltammetry (LSV) curves of the pretreated BiCuOS ($BiCuOS^R$), Bi_2O_3 ($Bi_2O_3{}^R$) and Bi_2S_3 ($Bi_2S_3{}^R$) were conducted to evaluate their eCO_2R performance over a potential range of -0.3 to -0.9 V_{RHE}. As shown in Fig. 2a, $BiCuOS^R$ achieves substantially higher current densities than $Bi_2O_3{}^R$ and $Bi_2S_3{}^R$, demonstrating its superior catalytic activity toward eCO_2R. To identify the products and their faradaic efficiencies (FEs) at different potentials, electrolysis at a variety of constant potentials was conducted from -0.3 to -1.1 V_{RHE}, and the resulting samples were collected for further analysis. As shown in Fig. 2b, the chronoamperometry curves of the samples display current densities that follow the same trend as the LSV measurements and remain stable, demonstrating the high electrochemical stability of the BiCuOS catalyst. Gas chromatography (GC) and ^1H nuclear magnetic resonance (NMR) (Fig. S7) analyses identify that formate is the primary product for the BiCuOS catalyst, accompanied by minor amounts of H_2 and CO gas. Notably, the $BiCuOS^R$ catalyst exhibits high selectivity towards formate production, with a $FE_{formate}$ exceeding 90% over a wide potential range from -0.3 to $-0.9V_{RHE}$. The maximum $FE_{formate}$ reaches approximately 96.6% at $-0.7V_{RHE}$. In contrast, the FE_{CO} and FE_{H2} were approximately 0.9% and 1.5%,

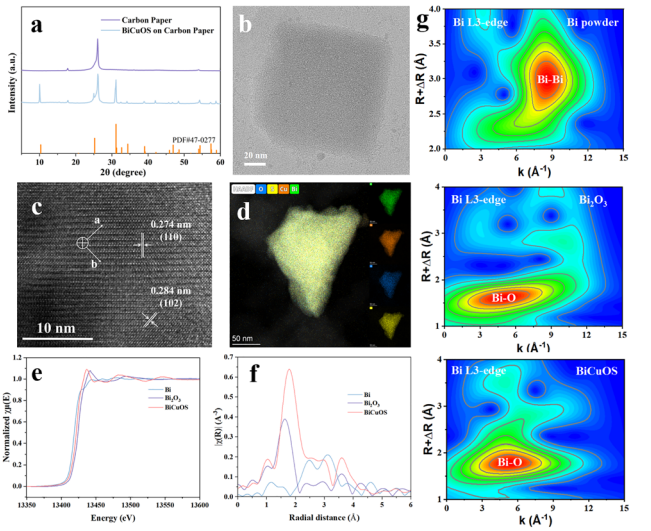

Fig. 1 (a) XRD patterns of the synthesized BiCuOS. (b) TEM image of a BiCuOS nanosheet. (c) HRTEM image of the synthesized BiCuOS along the [001] zone axis. (d) STEM-EDS elemental mapping of BiCuOS. XAFS characterization of the synthesised BiCuOS: (e) Bi L3-edge XANES spectra of synthesized BiCuOS and (f) the corresponding *R*-space radial distribution function diagram. (g) Wavelet transform of the k^2-weighted EXAFS spectra of the Bi L3-edge.

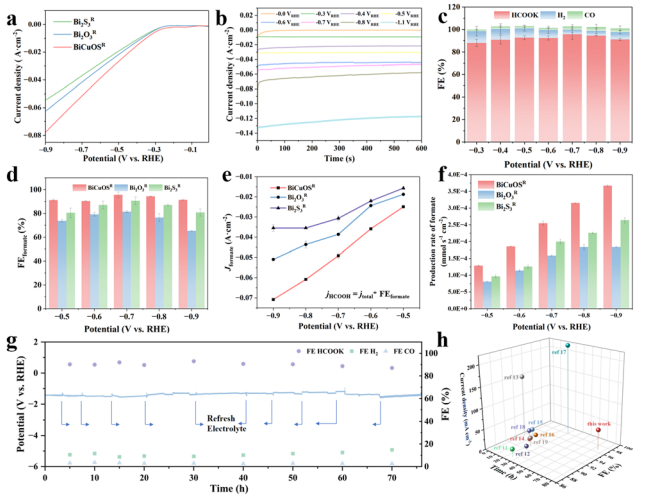

Fig. 2 (a) LSV curves among $BiCuOS^R$, $Bi_2O_3{}^R$ and $Bi_2S_3{}^R$. (b) Chronoamperometric curves of BiCuOS at different potentials with iR compensation in 0.5 M $KHCO_3$. (c) eCO_2R performance in 0.5 M $KHCO_3$ with iR compensation. FE of formate, CO and H_2 for BiCuOS Ns. (d) $FE_{formate}$, (e) partial current density and (f) production rate of formate for $BiCuOS^R$, $Bi_2O_3{}^R$ and $Bi_2S_3{}^R$ under iR-compensated conditions in 0.5 M $KHCO_3$. (g) Chronoamperometric stability test of BiCuOS at -1.45 V_{RHE} for 75 h without iR compensation in 0.5 M $KHCO_3$. (h) Comparison of stability time, $FE_{formate}$, and operating current density with those of reported oxidized Bi-based catalysts. All data with error bars are based on three independent replicates.

respectively (Fig. 2c). The $FE_{formate}$ for $BiCuOS^R$ is significantly higher than those for $Bi_2O_3{}^R$ ($FE_{formate}$ = 82%), $Bi_2S_3{}^R$ ($FE_{formate}$ = 91.8%) and Bi_2O_3-Bi_2S_3-Cu_2S^R ($FE_{formate}$ = 82%) across the tested potentials (Fig. 2d and Fig. S9–S11). Furthermore, the calculated formate partial current densities ($J_{formate}$) of $BiCuOS^R$ are significantly larger than those of $Bi_2O_3{}^R$ and $Bi_2S_3{}^R$ at the same potentials, reaching a maximum of 72.5 mA cm^{-2} at −0.9 V_{RHE} (Fig. 2e), with the highest formate production rate of 3.67 × 10^{-4} mmol s^{-1} cm^{-2} (Fig. 2f). These results indicate that BiCuOS NSs preferentially produce formate. During a 75-hour stability test at a constant current density of 50 mA cm^{-2}, the potential stabilizes at approximately −1.45 V_{RHE}, while the $FE_{formate}$ remains around 92% (Fig. 2g). These results underlie that BiCuOS can maintain outstanding formate selectivity over a wide potential window (> 90% from −0.4 to −0.9 V_{RHE}), outperforming other state-of-the-art oxidized Bi-based catalysts (Fig. 2h, Table S1).[11–19] The catalytic performance of BiCuOS was further evaluated in 1 M KOH. Details are discussed in the SI (Fig. S12).

Fig. 3a shows the XRD patterns of the BiCuOS catalyst before and after eCO_2R. The post-reaction pattern closely resembles that of the pristine sample, exhibiting no new diffraction peaks or shifts in peak positions. This confirms that the overall crystal structure is preserved and remains stable during catalysis. Furthermore, *quasi in situ* XRD patterns collected at different reaction times (Fig. 3b and Fig. S13 and S14) exhibit no noticeable changes in peak positions or intensities, indicating that the crystalline phase remains stable throughout the reaction process. *In situ* Raman spectra tested under different applied potentials consistently display the characteristic Bi–O vibrational peak at 151 cm^{-1}, with no evident disappearance or shift, suggesting that the Bi–O bonds do not undergo restructuring during the reaction.[20] Additionally, the signals associated with the Cu–S bond at 274 cm^{-1} also remain stable,[21] suggesting that all layers within the superlattice structure maintain their integrity throughout restructuring (Fig. 3c). XPS was further performed to investigate the chemical states of BiCuOS before and after eCO_2R (Fig. 3d, e and Fig. S15). XPS quantitative analysis indicates that the relative Bi/Cu/S composition remains close to the intrinsic framework stoichiometry after reaction (Table S2). The Bi–O layer structure is well maintained during the reaction, as also proved by synchrotron radiation XAFS. The XANES spectra reveal that both the Bi L3-absorption edge position exhibits minor shift toward lower energy, while the absorption edge position and the white-line features of $BiCuOS^R$ closely overlap with the Bi_2O_3 reference, suggesting that the oxidation state of Bi is preserved after the reaction (Fig. 3f). The FT-EXAFS results are discussed in the SI (Fig. S16). The structural stability of the BiCuOS catalysts is further supported by the SEM observations (Fig. S17). Details of the post-reaction characterizations of the comparative samples are provided in the SI (Fig. S18–S25). Although minor corrosion marks are observed on the surface of $BiCuOS^R$ after eCO_2R, the overall flake-like morphology is retained (Fig. 3g). Post-reaction HRTEM images reveal lattice spacings of 0.289 nm corresponding to the (102) plane (Fig. 3h), confirming preserved crystallographic features. Furthermore, EDS elemental mapping and line-scan analysis confirm the uniform and continuous distribution of Bi, Cu, O, and S throughout the nanosheets and along the scanned region, respectively (Fig. 3i and Fig. S26). ICP-OES analysis of the post-electrolysis electrolyte showed no leaching of Bi or Cu during eCO_2R (Table S3).

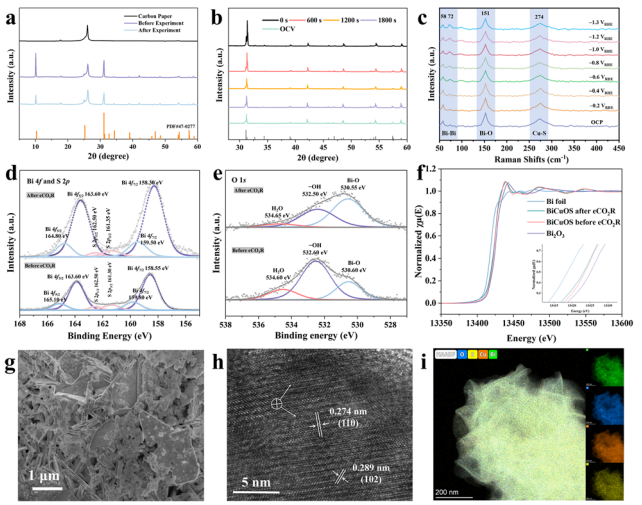

Fig. 3 (a) *Ex situ* XRD patterns and (b) time-resolved *quasi in situ* XRD patterns of BiCuOS NSs during eCO_2R in 0.5 M $KHCO_3$ as the electrolyte under a current density of 20 mA cm^{-2}. (c) Potential-dependent *in situ* SERS of the BiCuOS catalysts in 0.5 M $KHCO_3$ solution under CO_2 bubbling. (d) Bi 4f and S 2p, and (e) O 1s XPS spectra of BiCuOS before and after eCO_2R. (f) Bi L3-edge XANES spectra of the BiCuOS before and after eCO_2R. (g) SEM image, (h) HRTEM image, and (i) STEM-EDS elemental mapping of the BiCuOS after eCO_2R.

COHP analysis reveals that the bonding strength of the Bi–O bond in BiCuOS is significantly higher than that in Bi_2O_3 (Fig. 4a and b). Specifically, the ICOHP value of the Bi–O bond in BiCuOS is −3.27 eV, whereas the ICOHP of the Bi–O bond in Bi_2O_3 is only −0.91 eV. Even when compared with the strongest short Bi–O bonds in Bi_2O_3, the ICOHP of the Bi–O bond in BiCuOS remains slightly more negative. This result indicates a stronger Bi–O bonding interaction in BiCuOS, which is consistent with the enhanced stability of the Bi–O framework in BiCuOS. *In situ* attenuated total reflectance-Fourier transform infrared (ATR-FTIR) shows that clear absorption peaks are observed near 1400 cm^{-1}, which gradually intensified as the applied potential became more negative. These peaks correspond to the C–O stretching vibration of the *OCHO intermediate, indicating that *OCHO is the dominant reaction intermediate (Fig. 4c). Under CO_2-saturated conditions, *in situ* surface-enhanced Raman spectroscopy (SERS) recorded at different potentials reveals two key characteristic peaks. The peak at 1050 cm^{-1} corresponds to the $CO_3{}^{2-}$ intermediate and another peak at 1355 cm^{-1} is the signal of *OCHO (Fig. 4d and Fig. S27, S28).[22] These *in situ* results verify the formation of *OCHO in the reaction pathway and the conversion of *OCHO to *HCOOH is the rate-determining step. To further elucidate the reaction mechanism, DFT calculations were conducted. The surfaces and adsorption structures were generated on the LASPAI website,[23–26] and the adsorption configurations of reaction intermediates on different catalysts are presented in Fig. S33. The calculated transition state energy barrier shows that

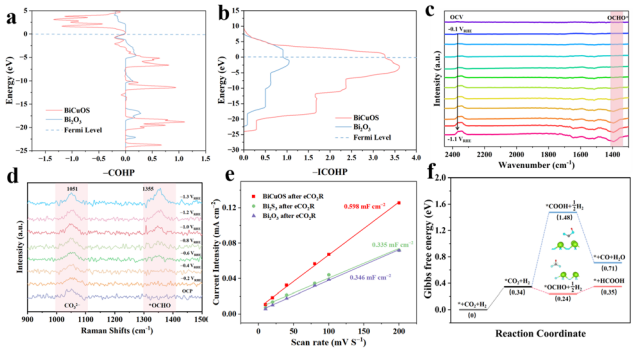

Fig. 4 COHP analysis of Bi–O bonding interactions in BiCuOS and Bi_2O_3. (a) Energy-resolved −COHP curves for the Bi–O bond in BiCuOS and Bi_2O_3. (b) Corresponding −ICOHP profiles as a function of energy. (c) *In situ* attenuated total reflectance-Fourier transform infrared (ATR-FTIR) of intermediates of BiCuOS catalysts during eCO_2R under CO_2 bubbling. (d) Potential-dependent *in situ* surface-enhance Raman spectroscopy (SERS) of BiCuOS catalysts in 0.5 M $KHCO_3$ solution under CO_2 bubbling. (e) Double–layer capacitance (C_{dl}) comparison among BiCuOS, Bi_2S_3 and Bi_2O_3 after eCO_2R. DFT calculations for the electrochemical reduction of CO_2 to formate process over BiCuOS. (f) Calculated free-energy diagram.

the *OCHO pathway exhibits the lowest barrier (0.24 eV), significantly lower than that of the competing *COOH route (1.48 eV) (Fig. 4f). This energetic preference suggests that the reaction predominantly follows the *OCHO intermediate pathway toward HCOOH formation.

In summary, the BiCuOS superlattice is systematically evaluated as a high-performance catalyst for eCO_2R. The material exhibits exceptional formate selectivity across a broad potential window (−0.3 to −0.9 V_{RHE}), achieving a maximum $FE_{formate}$ of 96.6% at −0.7 V_{RHE}. Remarkably, during a 75-hour stability test in neutral electrolyte, the potential stabilizes at −1.45 V_{RHE} under a constant current density of 50 mA cm^{-2}, while $FE_{formate}$ remains around 92%, highlighting its robust operational stability. Comprehensive characterization and calculations confirm the structural integrity of the Bi–O and Cu–S bonds, and the absence of catalyst phase transformation throughout the reaction. *In situ* ATR-SEIRAS identifies *OCHO as the key reaction intermediate, and DFT calculations indicate a lower energy barrier for its protonation to HCOOH, establishing this step as rate-determining. These results demonstrate that the BiCuOS superlattice not only serves as a stable and highly selective catalyst for eCO_2R to formate but also provides mechanistic insights into how a well-preserved Bi–O framework facilitates selective CO_2 reduction under practical conditions.

The manuscript was written through contributions of all authors. G. C., Y. X., Z. T., and W. C. conceived the project. G. C. and Z. T. designed and performed the experiments, analyzed the data, and wrote and edited the manuscript. Z. T. and W. C. edited the manuscript and discussed the scientific results as a supervisor. Y. X., Y. D., and L. F. characterized the morphology and composition of each catalyst using HRTEM and Raman spectra. J. C. carried out the DFT calculations. M. W., L. F., C. J., C. G., H. L. and B. T. edited the manuscript. W. C. provided resources as a supervisor. All authors have given approval to the final version of the manuscript.

Conflicts of interest

There are no conflicts to declare.

Data availability

The data supporting this article have been included as part of the supplementary information (SI). Supplementary information is available. See DOI: https://doi.org/10.1039/d6cc01492e.

Acknowledgements

This research is supported by the National Research Foundation, Prime Minister's Office, Singapore under its Campus for Research Excellence and Technological Enterprise (CREATE) programme *via* CREATE Thematic Programme in Decarbonisation (Development of advanced catalysts for electrochemical carbon abatement, Project Code: 370184872), and the AISI-NUS Joint Research Initiative Fund (A-8003323-00-00).

References

1 S. Deutz, D. Bongartz, B. Heuser, A. Kätelhön, L. Schulze Langenhorst, A. Omari, M. Walters, J. Klankermayer, W. Leitner, A. Mitsos, S. Pischinger and A. Bardow, Cleaner production of cleaner fuels: wind-to-wheel-environmental assessment of CO_2-based oxymethylene ether as a drop-in fuel, *Energy Environ. Sci.*, 2018, **11**, 331–343.
2 B. Parkinson, P. Balcombe, J. F. Speirs, A. D. Hawkes and K. Hellgardt, Levelized cost of CO_2 mitigation from hydrogen production routes, *Energy Environ. Sci.*, 2019, **12**, 19–40.
3 P. Li, F. Yang, J. Li, Q. Zhu, J. W. Xu, X. J. Loh, K.-W. Huang, W. Hu and J. Lu, Nanoscale Engineering of P-Block Metal-Based Catalysts Toward Industrial-Scale Electrochemical Reduction of CO_2, *Adv. Energy Mater.*, 2023, **13**, 2301597.
4 T. Dong, H. Li, Z. Wang, Y. Geng, R. Chang, X. Tian, J. Lai, S. Feng and L. Wang, Acidic electroreduction CO_2 to formic acid *via* interfacial modification of Bi nanoparticles at industrial-level current, *Nano Res.*, 2024, **17**, 5817–5825.
5 W. Ma, S. Xie, X.-G. Zhang, F. Sun, J. Kang, Z. Jiang, Q. Zhang, D.-Y. Wu and Y. Wang, Promoting electrocatalytic CO_2 reduction to formate via sulfur-boosting water activation on indium surfaces, *Nat. Commun.*, 2019, **10**, 892.
6 Q. Gong, P. Ding, M. Xu, X. Zhu, M. Wang, J. Deng, Q. Ma, N. Han, Y. Zhu, J. Lu, Z. Feng, Y. Li, W. Zhou and Y. Li, Structural defects on converted bismuth oxide nanotubes enable highly active electrocatalysis of carbon dioxide reduction, *Nat. Commun.*, 2019, **10**, 2807.
7 H. Hiramatsu, H. Yanagi, T. Kamiya, K. Ueda, M. Hirano and H. Hosono, Crystal Structures, Optoelectronic Properties, and Electronic Structures of Layered Oxychalcogenides MCuOCh (M = Bi, La; Ch = S, Se, Te): Effects of Electronic Configurations of M^{3+} Ions, *Chem. Mater.*, 2008, **20**, 326–334.
8 W. C. Sheets, E. S. Stampler, H. Kabbour, M. I. Bertoni, L. Cario, T. O. Mason, T. J. Marks and K. R. Poeppelmeier, Facile Synthesis of BiCuOS by Hydrothermal Methods, *Inorg. Chem.*, 2007, **46**, 10741–10748.
9 J. Gamon, D. Giaume, G. Wallez, J. B. Labégorre, O. I. Lebedev, R. Al Rahal Al Orabi, S. Haller, T. Le Mercier, E. Guilmeau, A. Maignan and P. Barboux, Substituting Copper with Silver in the BiMOCh Layered Compounds (M = Cu or Ag; Ch = S, Se, or Te): Crystal, Electronic Structure, and Optoelectronic Properties, *Chem. Mater.*, 2018, **30**, 549–558.
10 C. Zhang, J. He, R. McClain, H. Xie, S. Cai, L. N. Walters, J. Shen, F. Ding, X. Zhou, C. D. Malliakas, J. M. Rondinelli, M. G. Kanatzidis, C. Wolverton, V. P. Dravid and K. R. Poeppelmeier, Low Thermal Conductivity in Heteroanionic Materials with Layers of Homoleptic Polyhedra, *J. Am. Chem. Soc.*, 2022, **144**, 2569–2579.
11 T. Tran-Phu, R. Daiyan, Z. Fusco, Z. Ma, R. Amal and A. Tricoli, Nanostructured β-Bi_2O_3 Fractals on Carbon Fibers for Highly

Selective CO_2 Electroreduction to Formate, *Adv. Funct. Mater.*, 2020, **30**, 1906478.
12 P. Deng, H. Wang, R. Qi, J. Zhu, S. Chen, F. Yang, L. Zhou, K. Qi, H. Liu and B. Y. Xia, Bismuth Oxides with Enhanced Bismuth–Oxygen Structure for Efficient Electrochemical Reduction of Carbon Dioxide to Formate, *ACS Catal.*, 2020, **10**, 743–750.
13 P. Deng, F. Yang, Z. Wang, S. Chen, Y. Zhou, S. Zaman and B. Y. Xia, Metal–Organic Framework-Derived Carbon Nanorods Encapsulating Bismuth Oxides for Rapid and Selective CO2 Electroreduction to Formate, *Angew. Chem., Int. Ed.*, 2020, **59**, 10807–10813.
14 Y. Wang, Y. Li, J. Liu, C. Dong, C. Xiao, L. Cheng, H. Jiang, H. Jiang and C. Li, $BiPO_4$-Derived 2D Nanosheets for Efficient Electrocatalytic Reduction of CO_2 to Liquid Fuel, *Angew. Chem., Int. Ed.*, 2021, **60**, 7681–7685.
15 J. Duan, T. Liu, Y. Zhao, R. Yang, Y. Zhao, W. Wang, Y. Liu, H. Li, Y. Li and T. Zhai, Active and conductive layer stacked superlattices for highly selective CO_2 electroreduction, *Nat. Commun.*, 2022, **13**, 2039.
16 S. Liu, X. F. Lu, J. Xiao, X. Wang and X. W. Lou, Bi_2O_3 Nanosheets Grown on Multi-Channel Carbon Matrix to Catalyze Efficient CO_2 Electroreduction to HCOOH, *Angew. Chem., Int. Ed.*, 2019, **58**, 13828–13833.
17 Z. Chen, K. Mou, X. Wang and L. Liu, Nitrogen-Doped Graphene Quantum Dots Enhance the Activity of Bi_2O_3 Nanosheets for Electrochemical Reduction of CO_2 in a Wide Negative Potential Region, *Angew. Chem., Int. Ed.*, 2018, **57**, 12790–12794.
18 C.-C. Miao and G.-Q. Yuan, Morphology-Controlled Bi_2O_3 Nanoparticles as Catalysts for Selective Electrochemical Reduction of CO_2 to Formate, *ChemElectroChem*, 2018, **5**, 3741–3747.
19 X. Feng, H. Zou, R. Zheng, W. Wei, R. Wang, W. Zou, G. Lim, J. Hong, L. Duan and H. Chen, Bi_2O_3/BiO_2 nanoheterojunction for highly efficient electrocatalytic CO_2 reduction to formate, *Nano Lett.*, 2022, **22**, 1656–1664.
20 X. Yan, L. Pan, Y. Mao, H. Kang, Z. Song, X. Zhang, X. Yan, W. Ma, B. Liu and Y. Zhao, Carbon quantum dots decorated $Bi_4O_5I_2$ with greatly improved visible-light photocatalytic performance, *Desalin. Water Treat.*, 2021, **230**, 411–418.
21 V. Vinayakumar, S. Shaji, D. Avellaneda, J. A. Aguilar Martínez and B. Krishnan, Copper antimony sulfide thin films for visible to near infrared photodetector applications, *RSC Adv.*, 2018, **8**, 31055–31065.
22 H. Shen, Y. Zhao, L. Zhang, Y. He, S. Yang, T. Wang, Y. Cao, Y. Guo, Q. Zhang and H. Zhang, *In Situ* Constructuring of Copper-Doped Bismuth Catalyst for Highly Efficient CO_2 Electrolysis to Formate in Ampere-Level, *Adv. Energy Mater.*, 2023, **13**, 2202818.
23 S.-D. Huang, C. Shang, P.-L. Kang, X.-J. Zhang and Z.-P. Liu, LASP: Fast global potential energy surface exploration, *WIREs Comput. Mol. Sci.*, 2019, **9**, e1415.
24 P.-l Kang, C. Shang and Z.-P. Liu, Recent implementations in LASP 3.0: Global neural network potential with multiple elements and better long-range description, *Chin. J. Chem. Phys.*, 2021, **34**, 583–590.
25 C. Shang and Z.-P. Liu, Stochastic Surface Walking Method for Structure Prediction and Pathway Searching, *J. Chem. Theory Comput.*, 2013, **9**, 1838–1845.
26 C. Shang, X.-J. Zhang and Z.-P. Liu, Stochastic surface walking method for crystal structure and phase transition pathway prediction, *Phys. Chem. Chem. Phys.*, 2014, **16**, 17845–17856.